

THE CIRCUMGALACTIC MEDIUM OF eBOSS EMISSION LINE GALAXIES:
SIGNATURES OF GALACTIC OUTFLOWS IN GAS DISTRIBUTION AND KINEMATICSTING-WEN LAN¹ AND HOUJUN MO^{2,3}*Draft version February 28, 2024*

ABSTRACT

We study the distribution and kinematics of the cool circumgalactic medium (CGM) of emission line galaxies (ELGs) traced by metal absorption lines. Using about 200,000 ELGs from SDSS-IV eBOSS and half a million background quasars from SDSS, we measure the median absorption strength of MgII and FeII lines in quasar spectra for impact parameters ranging from 10 kpc to 1 Mpc. For comparison we measure the same quantity around luminous red galaxies (LRGs). On scales greater than 100 kpc both ELGs and LRGs exhibit similar absorption profiles. However, metal absorption is 5-10 times stronger around ELGs on smaller scales. The metal absorption strength is anisotropic, with an excess along the minor-axis of the galaxies, indicating an outflow origin of the absorbing gas. The ratio between the velocity dispersion of the cool CGM and that of its host dark matter halo is about one for ELGs but about half for LRGs. These results show that the dichotomy of galaxy types is reflected in both the density distribution and kinematics of the CGM traced by metal absorption lines. Our results provide strong evidence that the CGM of ELGs is enriched by gas outflows generated by star formation.

Keywords: quasars: absorption lines, galaxies: halos, intergalactic medium

1. INTRODUCTION

Gas around galaxies, the circumgalactic media (CGM), contains information about gas accretion and outflows, important processes that drive the evolution of galaxies (Tumlinson et al. 2017, for a review). By probing the properties of the CGM and their connections with galaxies, one can hope to understand the influences of these mechanisms, thereby better understanding the formation and evolution of galaxies in general. To this end, absorption line spectroscopy has been a powerful tool to extract the properties of the CGM through its absorption line signatures in the spectra of background objects.

Since the first discovery of a pair of galaxy and metal absorber produced by the CGM (Bergeron 1986), many investigations about the relationships between galaxies and their surrounding gas have been carried out over a wide range of redshift and using samples of at most a few hundred galaxy-absorber pairs that are spectroscopically confirmed (e.g., Steidel et al. 1994; Churchill et al. 2005; Chen et al. 2010; Steidel et al. 2010; Tumlinson et al. 2011; Nielsen et al. 2013; Bordoloi et al. 2014; Liang & Chen 2014; Schroetter et al. 2016; Borthakur et al. 2016; Burchett et al. 2016; Ho et al. 2017; Heckman et al. 2017; Johnson et al. 2017; Rubin et al. 2018; Lopez et al. 2018). On the other hand, large survey datasets offer the opportunity to explore the connection between galaxies and the CGM statistically (e.g., Zibetti et al. 2007; Bordoloi et al. 2011; Ménard et al. 2011; Zhu & Ménard 2013a; Lan et al. 2014; Zhu et al. 2014; Peek et al. 2015; Huang et al. 2016). However, although interesting results have been

obtained from these studies, the properties of the gas around galaxies remain poorly constrained. In particular, a systematic investigation about the gas properties as a function of galaxy properties, which is required in order to understand the origin of the CGM, is still lacking.

In this paper, we intend to characterize the properties of gas around star-forming galaxies at redshift ~ 1 by making use of the largest emission line galaxy (ELGs) catalog observed by the Extended Baryon Oscillation Spectroscopic Survey (eBOSS, Dawson et al. 2016) in Sloan Digital Sky Survey IV (SDSS IV, Blanton et al. 2017). To this end, we cross-correlate the flux-decrement in the background quasar spectra with the presence of ELGs, and obtain the radial distribution and kinematics of the cool circumgalactic gas of star-forming galaxies. The structure of the paper is as follows. Our data analysis is described in Section 2, and our results are presented in Section 3. The implications of our results are discussed in Section 4, and we summarize in Section 5. Throughout the paper we adopt a flat Λ CDM cosmology with $h = 0.7$ and $\Omega_M = 0.3$.

2. DATA ANALYSIS

We study the properties of the CGM traced by metal absorption lines imprinted in the background quasar spectra. Our analysis is based on two spectroscopic galaxy samples provided by SDSS as foreground galaxies: (1) emission line galaxies (ELGs) and (2) luminous red galaxies (LRGs), using all the SDSS quasars as background objects. In the following, we describe in detail the samples and method for our analysis.

2.1. Datasets

Emission line galaxies - We use the emission line galaxy (ELGs) catalog compiled from the SDSS-IV eBOSS survey (Blanton et al. 2017; Dawson et al. 2016). This survey aims to detect star-forming galaxies with

¹ Kavli IPMU, the University of Tokyo (WPI), Kashiwa 277-8583, Japan

² Physics Department and Center for Astrophysics, Tsinghua University, Beijing 10084, China

³ Department of Astronomy, University of Massachusetts, LGRT-B619E, 710 North Pleasant Street, Amherst, MA, 01003, USA

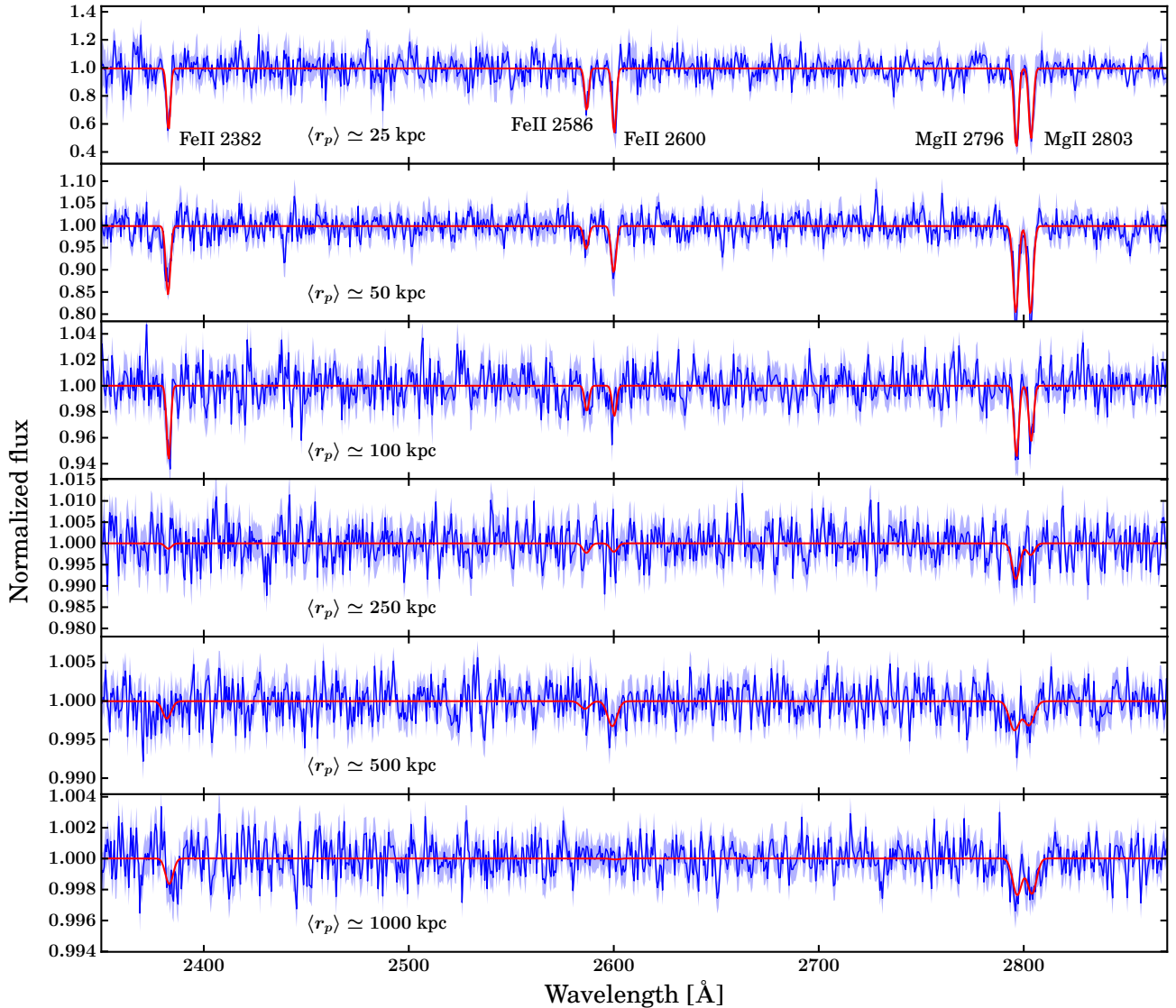


Figure 1. Example of median composite spectra of background quasars at rest-frame of ELGs as a function of r_p . The spectra and the best-fit MgII/FeII absorption lines are shown with blue and red solid lines, respectively. The blue shaded regions illustrate the bootstrapping uncertainties of the spectra. Note that the scale of y-axis changes as a function of r_p . The noise level of the composite spectrum at ~ 1000 kpc is about 10^{-3} of the continuum.

strong emission lines in the redshift range 0.8-1.0 and use them as tracers of the large-scale structure to investigate the baryonic acoustic oscillations. The galaxies are targeted from images obtained by the DECam Legacy Survey (Dey et al. 2018)⁴ with photometric selections that maximize the survey efficiency (Comparat et al. 2016; Raichoor et al. 2016). The spectra of the ELGs are obtained by the BOSS spectrograph (Smee et al. 2013) on the APO 2.5-meter SDSS telescope (Gunn et al. 2006) and processed by the SDSS spectroscopic pipeline (Bolton et al. 2012)⁵, which automatically estimates the redshifts of galaxies and derives the properties of emission lines (Hutchinson et al. 2016).

We select ELGs with redshifts greater than 0.4 with

reliable redshift estimation (Comparat et al. 2016). This yields a total of about 180,000 ELGs in the redshift range between 0.4 and 1.5, with a median value about 0.85. The typical uncertainty of the redshift estimate is about 20 km/s.

The ELGs have a typical stellar mass of about $3 \times 10^{10} M_\odot$ (Raichoor et al. 2017) and are hosted by dark matter halos with a typical mass of about $1.5 \times 10^{12} M_\odot$ (Favole et al. 2016). Based on their [OII] $\lambda 3727$ luminosities and the conversion model given by Kennicutt (1998), the ELGs have star formation rates (SFR) ranging from 1 to $20 M_\odot/\text{yr}$, with a median value of about $8 M_\odot/\text{yr}$. We note that the [OII] luminosities are not corrected for dust reddening.

Luminous red galaxies - We use the sample of luminous red galaxies (LRGs) provided by SDSS DR14 data release (Abolfathi et al. 2018) from the BOSS (Dawson

⁴ <http://legacysurvey.org/>

⁵ Version 5-10-7

Table 1
MgII rest equivalent widths around ELGs (upper part) and LRGs (lower part)

| r_p bin [kpc] | $\langle r_p \rangle$ | N_{spec} | $\langle W_{\text{MgII}} \rangle$ [Å] | $\sigma(\langle W_{\text{MgII}} \rangle)$ | $\langle W_{\lambda 2796} \rangle$ [Å] | $\sigma(\langle W_{\lambda 2796} \rangle)$ | $\langle W_{\lambda 2803} \rangle$ [Å] | $\sigma(\langle W_{\lambda 2803} \rangle)$ |
|-----------------|-----------------------|-------------------|---------------------------------------|---|--|--|--|--|
| (10, 28] | 23 | 11 | 2.830 | 0.243 | 1.529 | 0.135 | 1.301 | 0.142 |
| (28, 40] | 34 | 27 | 2.491 | 0.372 | 1.349 | 0.246 | 1.142 | 0.182 |
| (40, 56] | 50 | 50 | 1.307 | 0.175 | 0.647 | 0.121 | 0.660 | 0.080 |
| (56, 78] | 69 | 105 | 0.622 | 0.106 | 0.355 | 0.066 | 0.267 | 0.065 |
| (78, 110] | 95 | 183 | 0.287 | 0.050 | 0.161 | 0.033 | 0.127 | 0.029 |
| (110, 155] | 134 | 406 | 0.113 | 0.045 | 0.056 | 0.024 | 0.057 | 0.034 |
| (155, 218] | 190 | 774 | 0.030 | 0.030 | 0.023 | 0.021 | 0.006 | 0.027 |
| (218, 307] | 266 | 1571 | 0.052 | 0.023 | 0.040 | 0.014 | 0.012 | 0.016 |
| (307, 431] | 375 | 2946 | 0.044 | 0.019 | 0.017 | 0.015 | 0.027 | 0.016 |
| (431, 606] | 527 | 5902 | 0.044 | 0.013 | 0.024 | 0.010 | 0.019 | 0.009 |
| (606, 853] | 739 | 11512 | 0.022 | 0.010 | 0.016 | 0.007 | 0.006 | 0.007 |
| (853, 1200] | 1040 | 22999 | 0.025 | 0.006 | 0.013 | 0.004 | 0.012 | 0.004 |
| (10, 28] | 22 | 46 | 0.500 | 0.155 | 0.273 | 0.098 | 0.227 | 0.098 |
| (28, 40] | 35 | 75 | 0.447 | 0.193 | 0.234 | 0.127 | 0.214 | 0.112 |
| (40, 56] | 48 | 157 | 0.550 | 0.093 | 0.278 | 0.062 | 0.272 | 0.050 |
| (56, 78] | 68 | 362 | 0.250 | 0.052 | 0.150 | 0.031 | 0.100 | 0.028 |
| (78, 110] | 95 | 670 | 0.290 | 0.043 | 0.181 | 0.031 | 0.108 | 0.027 |
| (110, 155] | 135 | 1396 | 0.135 | 0.027 | 0.078 | 0.015 | 0.057 | 0.017 |
| (155, 218] | 189 | 2665 | 0.100 | 0.023 | 0.060 | 0.017 | 0.040 | 0.015 |
| (218, 307] | 266 | 5542 | 0.098 | 0.014 | 0.053 | 0.009 | 0.045 | 0.008 |
| (307, 431] | 380 | 12253 | 0.053 | 0.011 | 0.031 | 0.009 | 0.022 | 0.010 |
| (431, 606] | 526 | 28672 | 0.041 | 0.010 | 0.024 | 0.006 | 0.017 | 0.005 |
| (606, 853] | 739 | 56189 | 0.028 | 0.006 | 0.015 | 0.004 | 0.012 | 0.004 |
| (853, 1200] | 1041 | 110921 | 0.018 | 0.004 | 0.009 | 0.002 | 0.009 | 0.002 |

et al. 2013) and eBOSS (Prakash et al. 2016; Dawson et al. 2016) surveys. We select LRGs with redshifts greater than 0.4 and with redshift uncertainties smaller than 35 km/s. This yields a sample of about 760,000 LRGs, with median redshift of about 0.55. The typical stellar and halo masses of the LRGs are $\sim 10^{11.2} M_{\odot}$ and $\sim 10^{13.5} M_{\odot}$, respectively (e.g., White et al. 2011; Zhai et al. 2017). We note that while the MgII absorption around LRGs has been measured by Zhu et al. (2014) with a method similar to the one used here, we repeat the analysis with the latest sample (1) to obtain the FeII absorption which is not provided by Zhu et al. (2014), and (2) as a consistent check between the new data and previous ones.

Background quasars - For background objects, we use the SDSS DR14 quasar catalog (Abolfathi et al. 2018; Pâris et al. 2017), which contains all the quasars observed by the SDSS surveys. We select quasar-galaxy pairs that have projected distances smaller than 1.2 Mpc and have the quasar redshift higher than galaxy redshift by at least 0.1. This selection yields in total about 70,000 ELG-quasar pairs and 320,000 LRG-quasar pairs.

2.2. Method

We measure the average MgII and FeII absorption strengths (tracers of cool gas with $T \sim 10^4$ K) in the quasar spectra as functions of the impact parameter, r_p , defined to be the distance between the galaxy and the line of sight to its paired quasar. We follow the procedure in Zhu & Ménard (2013b) to estimate the absorption line strengths. We first model and remove spectral features in the quasar spectra that are intrinsic to quasars, using the quasar eigen-spectra provided by Zhu & Ménard (2013b), together with a dimensional reduction technique, called non-negative matrix factorization (NMF, Lee & Seung

2001), as implemented by Zhu (2016)⁶. Intermediate-scale fluctuations are removed by a median filter with a width of 71 pixels. We also remove the systematic features originated from the SDSS pipeline in the observer frame (Lan et al. 2018). Finally, we combine the continuum-normalized spectra of background quasars at the rest-frame of the foreground galaxies to obtain the composite spectra, which have higher S/N than the original individual spectra. A median estimator is used to avoid the impacts of outliers. We found that using a robust mean estimator yields consistent results. To make the composite spectra, we use pixels of quasar spectra with S/N greater than 3; including pixels with lower S/N does not enhance the quality of the final composite spectra. With this S/N selection, the composite spectra are made with $\sim 70\%$ of total galaxy-quasar pairs effectively. A similar method has been used in the analyses of gas absorption at both high (Steidel et al. 2010) and low (Zhu & Ménard 2013a) redshifts, as well as using galaxies as background sources (Bordoloi et al. 2011).

Figure 1 shows examples of the median composite spectra as a function of the impact parameter from ELGs. The shaded regions show the uncertainties of the composite spectra from 200 bootstrap samples. Note that the scale of vertical axis changes with the impact parameter. Note also that the signal-to-noise ratio of the composite spectra per spectral element is about 1000 at $r_p \sim 1000$ kpc.

We measure the rest equivalent widths of the MgII $\lambda\lambda 2796$, 2803 and FeII $\lambda\lambda 2600$, 2586, 2382 lines by fitting the spectra to Gaussian profiles with their amplitudes as free parameters. Since MgII and FeII lines trace gas clouds with the same physical properties and velocities (e.g., Churchill & Vogt 2001; Churchill et al.

⁶ The code can be found at <https://github.com/guangtunbenzhu/NonnegMFPy>.

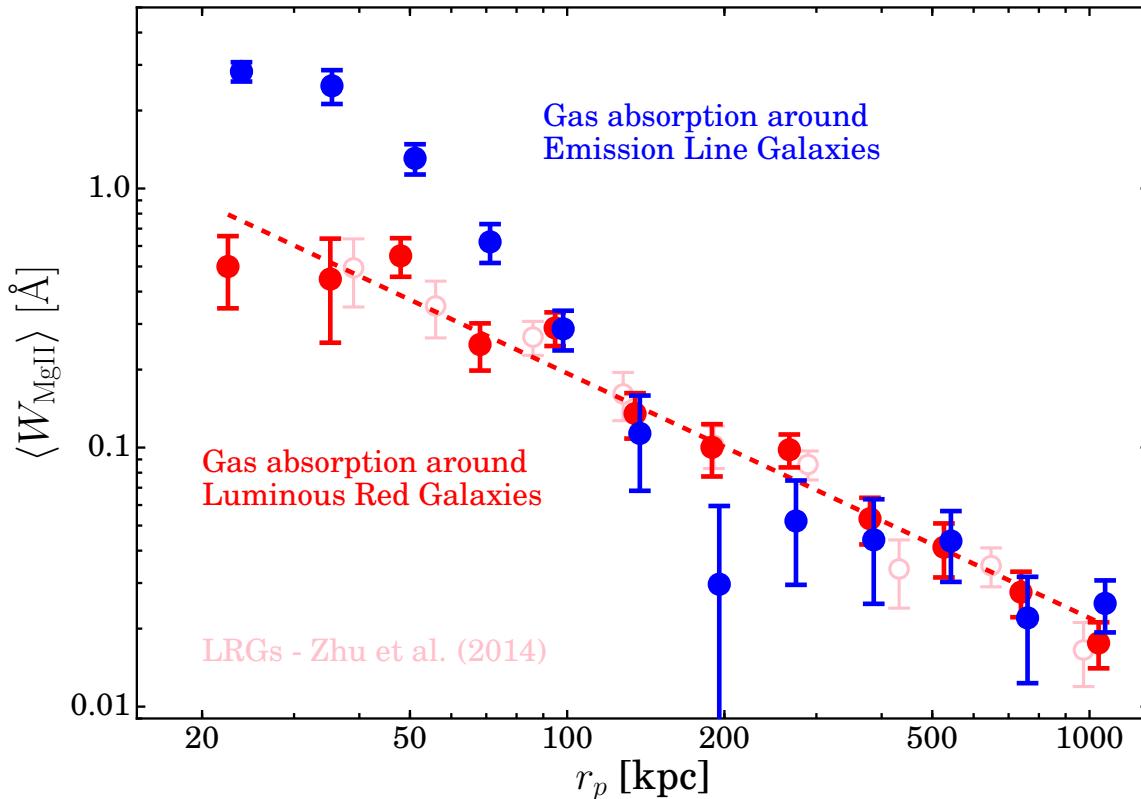


Figure 2. MgII rest equivalent width, the sum of MgII λ 2796 and λ 2803 lines, as a function of r_p . The gas profiles of ELGs and LRGs are shown with blue and red data points, respectively. The pink open circles show the LRG measurements from Zhu et al. (2014).

2003), we fit all the line widths with a single velocity dispersion parameter. The uncertainties of the rest-frame equivalent widths and velocity dispersion are estimated by bootstrapping the sample 200 times. Examples of the best-fit Gaussian profiles are shown with red solid lines in Figure 1.

MgII absorption lines have been detected individually in random quasar sightlines, and their rest equivalent width distribution is found to follow roughly an exponential distribution (e.g., Nestor et al. 2005; Zhu & Ménard 2013b). For a MgII absorber with rest equivalent width greater than 0.4 \AA , the absorption line is mostly saturated and therefore, the rest equivalent width reflects a combination of the internal velocity dispersion of the system and its column density. The probability to detect these absorbers around galaxies, namely the covering fraction, depends on the galaxy population as well as on the impact parameter from the galaxies (e.g., Chen et al. 2010; Nielsen et al. 2013; Lan et al. 2014). Since our composite spectra are made by combining random background quasar spectra *without prior knowledge* about individual metal absorbers, the measured average rest equivalent width, $\langle W_{\text{MgII}} \rangle$, reflects the summation of the product between the covering fraction and the absorption strength over individual MgII absorbers:

$$\langle W_{\text{MgII}} \rangle = \sum_i f_c(W_i^l < W_{\text{MgII},i} < W_i^u, r_p) \times \hat{W}_{\text{MgII},i}, \quad (1)$$

where $f_c(W_i^l < W_{\text{MgII},i} < W_i^u, r_p)$ is the covering fraction of absorbers with strength in $[W_i^l, W_i^u]$ at a given im-

pact parameter r_p , and $\hat{W}_{\text{MgII},i}$ is the average strength. Thus, even if $\langle W_{\text{MgII}} \rangle$ measured from our composite spectra appears to be unsaturated ($W < 0.4 \text{ \AA}$), it may be due to the combination of a low covering fraction with strongly saturated absorbers. This is consistent with the fact that the line ratio between MgII λ 2796 and λ 2803 is larger than 0.5 at scales $> 200 \text{ kpc}$ (see Fig. 1), even though the rest equivalent widths are small, suggesting that the average absorption is indeed dominated by strong saturated absorbers. Consequently, a direct conversion from the measured rest equivalent width to a column density may result in an underestimation of the metal abundance. In the following, we will first present our results in terms of the median rest equivalent width obtained from the composite spectra (Section 3), and then discuss the covering fraction and gas mass inferred from them (Section 4).

3. RESULTS

3.1. Gas distribution traced by MgII/FeII absorption lines

We measure the radial distribution of gas traced by MgII/FeII absorption lines. Figure 2 shows the median rest equivalent widths of the sum of MgII λ 2796 and MgII λ 2803 lines around ELGs and LRGs as functions of the impact parameter. The individual measurements are listed in Table 1 for reference.

It can be seen that the MgII absorption strength around both ELGs and LRGs decreases monotonically with r_p . For ELGs, there seems to be a change in slope at $r_p \sim 100 \text{ kpc}$: the absorption profile is roughly a

power law, $W \propto r_p^{-1}$ at larger r_p , and the profile is steeper, $r_p^{-1.5}$, at smaller r_p . In contrast, the MgII absorption profile around LRGs, shown by the red data points, can be described by a single power-law, $W \propto r_p^{-\alpha}$ with $\alpha = -0.94 \pm 0.05$, as illustrated by the red dashed line. The absorption profile around LRGs obtained here is consistent with the measurements of Zhu et al. (2014) (shown by the pink open circles), demonstrating the robustness of the observational results. In addition, our measurements extend the profile to $r_p < 30$ kpc.

At $r_p > 100$ kpc the gas absorption profile around ELGs is consistent with that around LRGs, but the amplitude is slight lower, by about 85%, albeit the large uncertainties. This difference in amplitude at $r_p > 100$ kpc may be due to that ELGs and LRGs reside in dark matter halos with average masses of $\sim 10^{12} M_\odot$ and $\sim 10^{13.5} M_\odot$, respectively. However, measurements with higher S/N are required to test this picture. At $r_p < 100$ kpc, the absorption profile around ELGs deviates significantly from the power law extrapolated from larger scales, and the absorption equivalent width is about a factor of 5-10 as large as that around LRGs. Such a trend is also observed in the FeII absorption profiles.

If we scale r_p by the corresponding halo virial radius, R_v , the small scale difference between ELGs and LRGs will be enhanced. This result indicates that the excess of MgII absorption around ELGs is limited in their host halos, likely due to gas outflows produced by the star formation activities in central galaxies (e.g. Bordoloi et al. 2011; Lan et al. 2014). This result demonstrates that the properties of galaxies is reflected in their surrounding cool gas.

3.2. Correlation with star-formation rate

To investigate how the absorption strength depends on the properties of galaxies, we separate the ELGs into two subsamples in SFR, one with $SFR > 10 M_\odot/\text{yr}$ and the other $SFR < 10 M_\odot/\text{yr}$, and measure their absorption properties. As shown in the two panels of Figure 3, the MgII and FeII absorption strengths at $r_p < 50$ kpc both increase with SFR. Comparing the average absorption strengths around ELGs with that around LRGs and passive galaxies of similar stellar masses (Rubin et al. 2018), one can see that the trend with SFR extends to red galaxies that have very low star formation rates. Nevertheless, the absorption strengths of the two subsamples are consistent with each other at $r_p > 50$ kpc. This trend is consistent with previous results obtained by Bordoloi et al. (2011), Lan et al. (2014), and Rubin et al. (2018). Our result demonstrates that the correlation between the SFR of galaxies and the properties of the circumgalactic gas is reflected not only in the MgII absorption, but also in the FeII absorption in the inner region of the CGM.

3.3. Dependence on azimuthal angle

The dependence of the metal absorption profile on the azimuthal angle, ϕ , defined to be the angle between the minor axis of the galaxy and the impact parameter vector of the background quasar, provides further insights into the origin of the circumgalactic gas. For example, gas clouds driven by gas outflows from a star-forming galaxy are expected to be preferentially along the minor axis

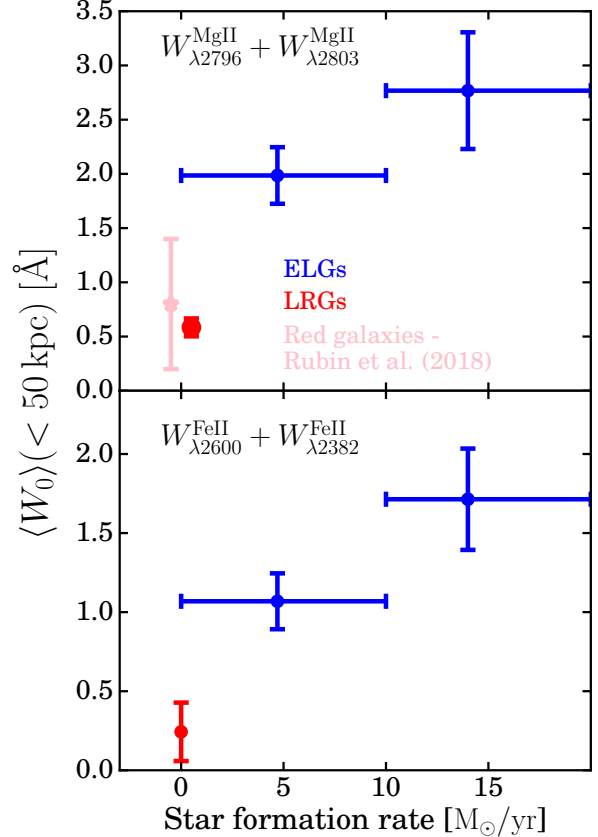


Figure 3. Absorption properties as a function of star-formation rate obtained from systems with impact parameters within 50 kpc. *Top:* the total width of the MgII $\lambda 2796$ and MgII $\lambda 2803$ lines. The same measurements around LRGs and red galaxies Rubin et al. (2018) are shown in red and pink, respectively. *Bottom:* the total width of the FeII $\lambda 2600$ and FeII $\lambda 2382$ lines. The results show that both the MgII and FeII absorption strengths are correlated with the SFR of the host galaxies.

of the galaxy (Veilleux et al. 2005, for a review), while cooling gas from a hot gaseous halo should have a more isotropic distribution. To investigate such dependence, we use the photometric information from DECaLS DR5 catalog (Dey et al. 2018) and select ELGs that are best-fitted by exponential disk profiles as determined by *The Tractor*⁷ (Lang et al. 2016) (See also Section 8 in Dey et al. 2018). This selection reduces the sample size by $\sim 60\%$. In short, the Tractor adopts a forward modeling approach by convolving modeled profiles with the point spread function of each individual exposure and finds the best-fit model profile that minimizes the residuals of all images. The algorithm only classifies extended objects into exponential disk profiles when the exponential disk profiles improve the fits by more than 3σ in comparison to round exponential profiles. We use the image shape parameters provided by *the Tractor* to estimate the azimuthal angles for individual galaxy-quasar pairs and the corresponding uncertainties, which are typically 5-10 degrees.

Figure 4 shows the MgII and FeII absorption strength as a function of r_p in two azimuthal angle bins, one with $\phi \in [0^\circ, 45^\circ)$ and the other with $\phi \in [45^\circ, 90^\circ]$ (see the

⁷ <https://github.com/dstndstn/tractor>

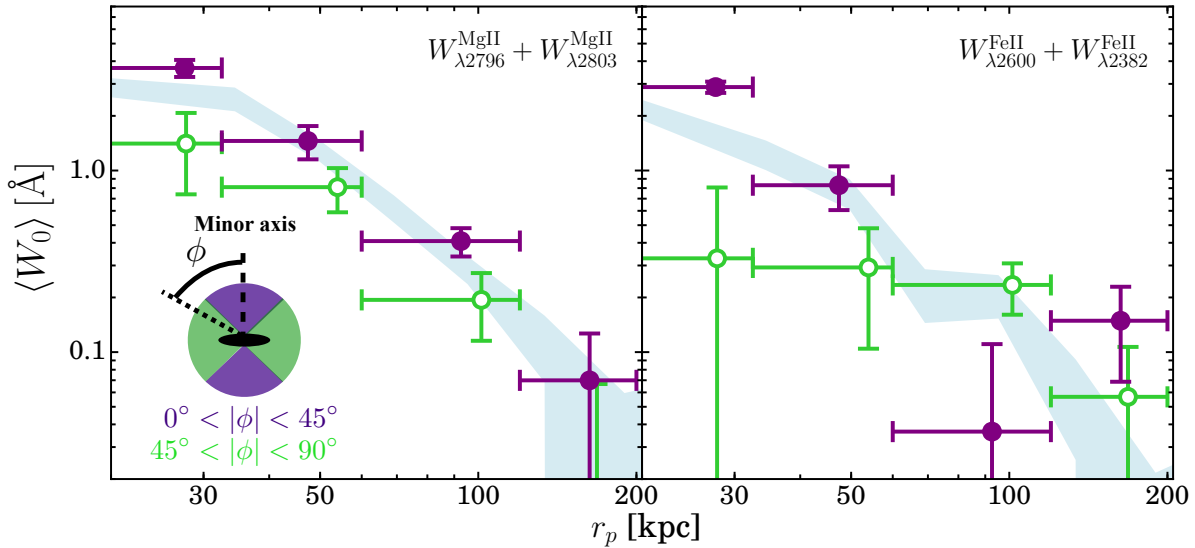


Figure 4. Dependence of the absorption profile on the azimuthal angle, ϕ , between the impact-parameter vector and the semi-minor axis of ELGs with exponential disk profiles. *Left:* the total width of the MgII λ 2796 and MgII λ 2803 lines. *Right:* the total width of the FeII λ 2600 and FeII λ 2382 lines. The purple and green data points show the absorption strengths along minor and major axis respectively. The blue bands show the measurements obtained by averaging over all directions.

cartoon plotted in the left panel for the relevant geometry). The SFR distributions of ELGs in the two bins are consistent with each other. As one can see, the MgII and FeII absorption strengths at $r_p < 50$ kpc are about 2 times larger along the minor axis of ELGs (purple) than along the major axis (green). At larger r_p , the absorption strengths for the two azimuthal angle bins are comparable. For reference, the blue bands show the measurements by averaging over all directions. As expected, the averages go through the measurements of the two azimuthal bins. We also perform similar measurements around LRGs and find no dependence on the azimuthal angle, consistent with the finding of Huang et al. (2016).

This orientation dependence of the MgII/FeII absorption around ELGs demonstrates that a significant fraction of the cool gas traced by the absorbers is likely contributed by outflows originated from the galaxies (disks). This result is consistent with those obtained earlier using smaller data sets from the HST, COSMOS, Keck, VLT and SDSS (e.g., Bordoloi et al. 2011; Bouché et al. 2012; Kacprzak et al. 2012; Lan et al. 2014). Other mechanisms, such as gas inflows and/or gas associated with satellite galaxies, are not expected to produce the azimuthal dependence observed, as we will discuss in §4.5.

Our results show that the metal absorption strength around ELGs is anisotropic. Based on the fact that the absorption strength along the minor axis is about two times stronger than that along the major axis, we infer that about 2/3 of the absorption is along the minor axis. Under the assumption that the metal absorption observed with $\phi \in [0^\circ, 45^\circ]$ is all due to outflows, this suggests that outflow gas contributes about 2/3 of the gas around ELGs within 50 kpc. This value should be considered as a lower limit, given that the opening angles of outflows may be larger than 45° . Moreover, the intrinsic azimuthal angle dependence is expected to be stronger than our measurements indicate, because galaxy shapes estimated from the ground-based observation may be af-

fected by seeing. In the near future, with the imaging data from the Euclid survey (Amiaux et al. 2012), one will be able to measure the azimuthal dependence of the gas absorption in more detail.

3.4. Gas Kinematics

In the composite spectra, the metal absorption lines in concern are contributed by multiple clouds with a range of velocities relative to the host galaxies. The line widths, therefore, reflect the line-of-sight velocity dispersion of the gas, σ_{gas} , around the galaxies, which is a convolution between the internal velocity dispersion of absorption systems and the relative velocity difference between the absorbers and the galaxies. In Figure 5, we show the best-fit velocity dispersion (obtained by a joint fit of 5 metal lines) of MgII/FeII gas clouds around ELGs as a function of the impact parameter, with effects produced by the SDSS spectral resolution and by the uncertainty in galaxy redshift subtracted in quadrature. The measured velocity dispersion of gas around ELGs is about 100 km/s from $r_p = 20$ to 100 kpc, and the results at larger r_p become uncertain. The blue shaded region shows the 1σ range of the best-fit gas velocity dispersion obtained by assuming a constant velocity dispersion. For comparison, the velocity dispersion of the gas around LRGs is shown in red. We note that our measured gas velocity dispersion around LRGs is consistent with those of Zhu et al. (2014) and Huang et al. (2016). The gas velocity dispersion around LRGs is about 60 km/s larger than that around ELGs.

Since ELGs reside in smaller dark matter halos than LRGs, it is informative to compare the gas velocity dispersion with that expected from the halo gravitational potential wells. Figure 6 shows the velocity dispersion of gas around galaxies as a function of halo mass. In addition to the measurements for ELGs and LRGs, shown by the blue and red data points, respectively, we also plot the dark matter velocity dispersion as a function of halo

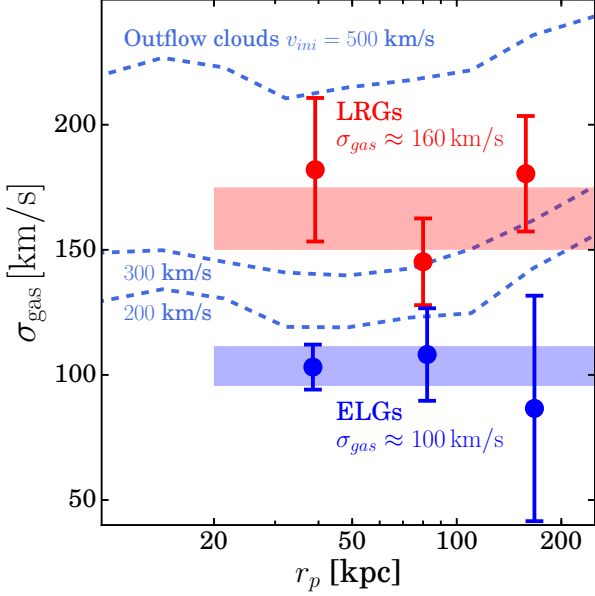


Figure 5. Line-of-sight gas velocity dispersion, σ_{gas} , as a function of r_p . The σ_{gas} around ELGs is about 100 km/s from 20 to 200 kpc, as shown by the blue data points. The blue shaded region shows the 1σ range of the best-fit σ_{gas} . The same quantity for LRGs is shown in red. The blue dashed lines show the expected velocity dispersion of gas particles based on a simple spherical outflow model described in the main text.

mass (e.g., Elahi et al. 2018),

$$\sigma_m \simeq 430 \left(\frac{M_{\text{halo}}}{10^{14} M_{\odot}} \right)^{1/3} \text{ km/s}, \quad (2)$$

as the blue dashed line. The velocity dispersion of the gas around ELGs is consistent with that of dark matter in their halos, while the gas velocity dispersion around LRGs is only about half of the σ_m , as shown by the red dotted line. Thus, we have gas velocity bias

$$\frac{\sigma_{\text{gas}}}{\sigma_m} \sim \begin{cases} 1 & \text{for ELGs;} \\ 0.5 & \text{for LRGs.} \end{cases} \quad (3)$$

A similar correlation between the kinematics of gas and galaxy types is also found in Nielsen et al. (2015) and Nielsen et al. (2016), where the authors measure the velocity dispersion of gas clouds relative to the column-density weighted median velocity. Figure 6 shows the velocity dispersion of MgII gas clouds around blue and red galaxies, derived from about 30 galaxy-absorber pairs given by Nielsen et al. (2015) and Nielsen et al. (2016), with the uncertainty estimated from bootstrapping. The halo masses are estimated from an abundance matching method (e.g., Conroy et al. 2006). Together with their data, the trend of gas velocity bias extends to even smaller halos. However, the methods and datasets used here and in Nielsen et al. (2015, 2016) are quite different, and so the comparisons may be uncertain. Clearly, a homogeneous dataset covering a wide range of halo masses and galaxy types is required to quantify the gas velocity bias as a function of halo mass. Nevertheless, our result shows clearly that the σ_{gas} of gas around star-forming and passive galaxies have very different behaviors with respect to that of dark matter, indicating that multiple

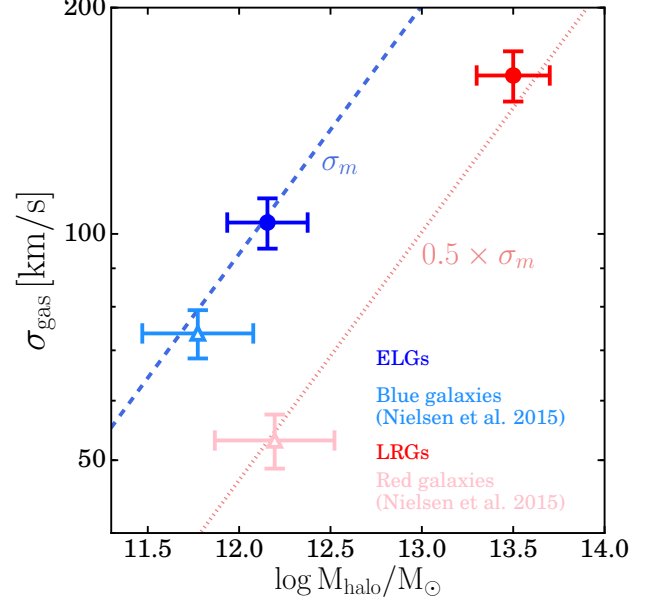


Figure 6. Line-of-sight gas velocity dispersion, σ_{gas} , as a function of halo mass and galaxy types. The σ_{gas} of ELGs and LRGs are shown by the blue and red data points. We find that the gas velocity dispersion around ELGs is consistent with the velocity dispersion of dark matter particles σ_m (Equation 2) shown by the blue dashed line, while the gas velocity dispersion around LRGs is aligned with 50% of the velocity dispersion of dark matter particles shown by the red dotted line. We also show similar measurements around blue and red galaxies derived from about 30 individual galaxy-absorber pairs from Nielsen et al. (2015, 2016), suggesting that gas in small halos may behave similarly.

mechanisms are driving the motion of the circum-galactic gas.

Let us first consider the possible mechanisms producing gas around passive galaxies. One possibility is that the gas clouds are produced by mass loss from stars in satellite galaxies and/or halo stars. In this case, the initial velocities of the clouds are expected to follow the virial velocity of the halo, in conflict with the observational result. However, in the presence of a diffuse hot halo, the cloud velocities are expected to be reduced by the interaction with hot ambient gas. Indeed, clouds with higher initial velocities are expected to be destroyed by hydrodynamic instabilities, such as Kelvin-Helmholtz and/or Rayleigh-Taylor instabilities, in shorter timescales, as the instability timescale is typically inversely proportional to the cloud velocity, $\propto V_{\text{cloud}}^{-1}$ (e.g. §8.5 in Mo et al. 2010). In addition, gas clouds are also expected to decelerate due to the ram pressure of hot gas. Thus, even if the clouds were produced with a velocity dispersion similar to that of the dark matter halo, these two mechanisms may work to reduce the gas velocity dispersion observed around passive galaxies. Alternatively, the gas clouds around passive galaxies may be produced by cooling gas from the hot halo. If the hot gaseous halo is static, the initial velocities of the clouds are expected to be small. The gravitational field of the dark matter halo will accelerate the gas clouds, but the clouds may get destroyed before they reach high velocities, leading to the low cloud velocity dispersion observed.

For star-forming galaxies, a large fraction of the clouds

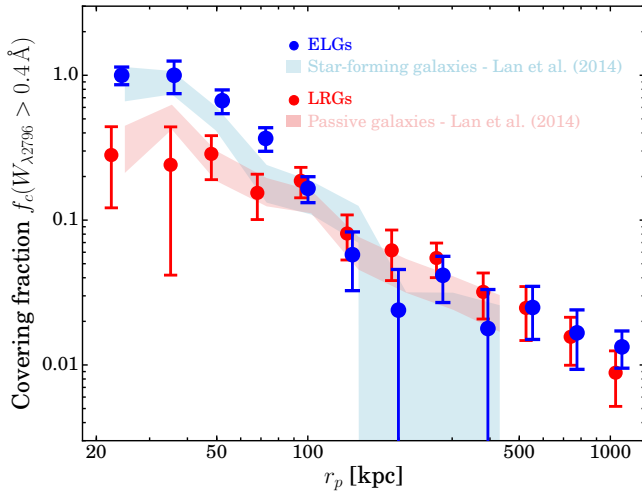


Figure 7. MgII covering fraction around galaxies. The blue data points and red squares show the covering fractions around ELGs and LRGs. The blue and red bands show the covering fractions estimated from Lan et al. (2014) by correlations with individual MgII absorbers and photometric galaxies.

may be produced by outflows, as such outflows have been observed ubiquitously (e.g., Heckman et al. 2000; Weiner et al. 2009; Steidel et al. 2010; Martin et al. 2012; Bordoloi et al. 2014; Rubin et al. 2014; Zhu et al. 2015; Heckman et al. 2015; Chisholm et al. 2016). Depending on the initial velocities of the outflows, these clouds may propagate to large distances from the halo center, inheriting large velocities. To demonstrate this possibility, we perform a simple simulation by ejecting particles at a radius of 1 kpc from the center of a dark matter halo that is assumed to have a NFW density profile (Navarro et al. 1996) with total mass of $10^{12} M_{\odot}$ and a concentration of 10. The ejection is assumed to have spherical symmetry and a constant rate over a period of 2 Gyr. We follow the motion of each ejected particle in the gravitational potential well of the halo, and calculate the velocity dispersion of ejected particles as a function of the impact parameter. The dashed faint blue lines in Figure 5 show the results obtained by assuming that the initial velocities following a normal distribution with a width 200 km/s, and with a mean velocity of 500 km/s, 300 km/s and 200 km/s, respectively. As one can see, outflow clouds may contribute significantly to the line of sight velocity dispersion, if the initial velocities sufficiently large. Note that the velocity dispersion obtained from our simple model should be considered as upper limits, as other mechanisms, such as ram pressure and hydrodynamic instabilities, are expected to reduce the velocity dispersion to be observed. In a forthcoming paper (Lan et al. in preparation), we will develop a more realistic model to test the ideas presented here.

4. IMPLICATIONS

4.1. The MgII covering fraction

The average MgII absorption around galaxies obtained above can be converted to the corresponding MgII covering fraction, f_c , as shown in Equation (1). To do this, we assume that the average MgII absorption around galaxies is dominated by strong MgII absorbers ($W_{\lambda 2796} > 0.4 \text{ \AA}$) and that the $W_{\lambda 2796}$ distribution around galaxies is sim-

ilar to the one observed towards random quasar sightlines. For simplicity, we approximate the average MgII absorption strength as

$$\langle W_{\lambda 2796} \rangle(r_p) \approx f_c(W_{\lambda 2796} > 0.4 \text{ \AA}, r_p) \times \hat{W}_{\lambda 2796}^{\text{MgII}}, \quad (4)$$

where $\langle W_{\lambda 2796} \rangle(r_p)$ is our average profile, and $\hat{W}_{\lambda 2796}^{\text{MgII}}$ is the average of $W_{\lambda 2796}$ obtained from individual absorbers towards random quasar sightlines. We use the incidence rate, $d^2 N/dW dz$, of individual MgII absorbers from Zhu & Ménard (2013b), and estimate $\hat{W}_{\lambda 2796}^{\text{MgII}}$ using systems with $W_{\lambda 2796} > 0.4 \text{ \AA}$. The corresponding $\hat{W}_{\lambda 2796}^{\text{MgII}}$ is $\sim 1 \text{ \AA}$. The estimated covering fraction from Equation (4) is shown in Figure 7 with the blue and red data points for ELGs and LRGs, respectively. Note that the initial covering fraction around ELGs at $< 40 \text{ kpc}$ exceeds 1, the maximum value for covering fraction, due to that MgII absorbers close to star-forming galaxies tend to have higher average rest equivalent widths than the global population (Lan et al. 2014). For such measurements, the covering fraction is set to be 1. The estimated covering fractions are compared with that derived from individual absorbers around blue and red galaxies (color shaded bands) (Lan et al. 2014). These two types of measurements yield consistent results, indicating that the assumption and the approximation adopted in Equation (4) are reasonable. This demonstrates that the average absorption around ELGs and LRGs is dominated by strong MgII absorbers with $W_{\lambda 2796} > 0.4 \text{ \AA}$, with only a negligible contribution from weaker components (see also Prochaska et al. 2014). These measurements for LRGs are consistent with Huang et al. (2016). The difference in the covering fractions between ELGs and LRGs shows that the MgII gas covering fraction is correlated with star formation activities in addition to halo mass as suggested by Churchill et al. (2013).

We have also performed a simulation to test the viability of using Equation (4) to estimate the covering fraction. To this end, we inject fake absorbers with $\hat{W}_{\lambda 2796}^{\text{MgII}} \sim 1 \text{ \AA}$ into the observed individual spectra and run our analysis to recover the input covering fraction. We find that the systematic uncertainty is about 20%, comparable to the statistical uncertainty. To better estimate the covering fraction, however, one needs to detect individual absorbers in each quasar sightline, instead of using Equation (4). We will perform such an analysis in the future.

4.2. Mass of circumgalactic neutral hydrogen

With the covering fraction obtained above, we can estimate the amount of hydrogen mass around ELGs and LRGs following Lan et al. (2014),

$$M_{\text{HI}}(r_p < r_{p, \text{max}}) \sim 2\pi m_{\text{H}} \int_{20 \text{ kpc}}^{r_{p, \text{max}}} \hat{N}_{\text{HI}} f_c(r_p) r_p dr_p, \quad (5)$$

where \hat{N}_{HI} is the neutral hydrogen column density traced by the MgII absorbers. Using the empirical relation between the rest equivalent width of MgII and N_{HI} derived by Lan & Fukugita (2017), we obtain $\hat{N}_{\text{HI}} \approx 3 \times 10^{19} \text{ cm}^{-2}$ for $\hat{W}_{\lambda 2796}^{\text{MgII}} \sim 1 \text{ \AA}$ at redshift 0.8. We perform the integration as a function of impact parameters and the enclosed

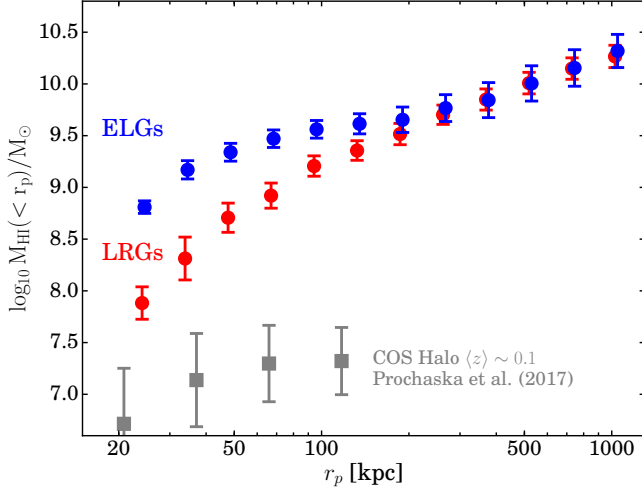


Figure 8. Cumulative neutral hydrogen mass around galaxies as a function of impact parameter.

neutral hydrogen mass obtained in this way is shown in Figure 8. As one can see, there is more neutral hydrogen around ELGs than around LRGs within $r_p \sim 100$ kpc, but the enclosed mass around the two populations becomes comparable at larger scales. The enclosed masses within the virial radii of ELGs (200 kpc) and LRGs (600 kpc) are $\sim 4 \times 10^9 M_\odot$ and $\sim 9 \times 10^9 M_\odot$, respectively. Compared with the halo masses of ELGs and LRGs, these neutral hydrogen masses imply that the HI mass fractions are

$$f \sim \begin{cases} 10^{-2.5} & \text{for star-forming galaxies;} \\ 10^{-3.5} & \text{for passive galaxies.} \end{cases} \quad (6)$$

Thus, the neutral hydrogen mass fraction within the halo around ELGs is about 10 times higher than that around LRGs. As shown in Lan & Fukugita (2017), the MgII absorption systems used in our analysis are predominantly neutral with $n_{\text{HI}}/n_{\text{H}} \sim 0.9$. Thus, the HI masses given above are approximately the same as the total hydrogen masses traced by MgII absorption lines.

We can compare the mass of the circumgalactic hydrogen obtained here with that at $z \sim 0.1$ obtained from the HST/COS-Halos survey (e.g. Stocke et al. 2013; Tumlinson et al. 2013; Werk et al. 2014; Prochaska et al. 2017). The COS-Halos results show that the neutral hydrogen is ubiquitously around galaxies, with a covering fraction nearly 100% from 10 kpc to 150 kpc (e.g., Tumlinson et al. 2013; Bordoloi et al. 2017). Accounting for the ionization effect, the estimated total cool CGM mass can be as high as $10^{11} M_\odot$ (Prochaska et al. 2017), more than 10 times higher than the mass traced by MgII absorption lines. However, the hydrogen gas detected in the COS-Halos survey is highly ionized, with an ionization correction factor greater than 100. To obtain the mass of neutral hydrogen gas detected in the COS-Halos survey, we take the data from Prochaska et al. (2017) and estimate the median N_{HI} for all types of galaxies as a function of impact parameters. We then calculate the neutral hydrogen mass using Equation (5) and assuming a covering fraction of 100% from 20 kpc to 150 kpc. We find that the total mass of neutral hydrogen detected by COS/Halos is only about $10^{7.5} M_\odot$, a factor of about 100 lower than the amount around ELGs shown

in Figure 8. This result indicates that the bulk of neutral hydrogen around galaxies is traced by strong MgII absorbers. The difference of the circumgalactic neutral hydrogen between ELGs and local galaxies may be caused by two factors. First, the number of COS-Halos sight-lines is not big enough to properly sample the cool dense clouds with relatively high HI column density and low covering fraction. Second, the amount of neutral hydrogen around galaxies decreases significantly from $z \sim 1$ to 0.1. At the moment, it is unclear which of the two is the right reason.

Our mass estimates also allow us to quantify the cosmic mass density of neutral hydrogen contributed from the CGM of ELGs ($r_p < 200$ kpc). To do this, we assume that all the star-forming galaxies with $M_* > 10^{10} M_\odot$ have similar gas profiles as ELGs and use the number density of star-forming galaxies, $n(\text{SFR} > 2 M_\odot/\text{yr}) \sim 10^{-2.6} \text{ Mpc}^{-3}$ at $z \sim 0.8$ from Moustakas et al. (2013). The cosmic mass density of neutral hydrogen around ELGs at $z \sim 0.8$ estimated in this way is

$$\Omega_{\text{HI}}^{\text{ELGs}} = \frac{n \times M_{\text{HI}}}{\rho_{\text{crit}}} \approx 1 \times 10^{-4}. \quad (7)$$

Using the incidence rate of individual MgII absorbers and the empirical relation between N_{HI} and $W_{\lambda 2796}$, previous studies (Kacprzak & Churchill 2011; Ménard & Fukugita 2012; Lan & Fukugita 2017) estimated the total mass density of neutral hydrogen traced by MgII absorbers to be $\Omega_{\text{HI}}^{\text{MgII}} \approx 1.5 \times 10^{-4}$ around redshift 1. This suggests that more than 60% of the individual MgII absorbers observed towards random quasar sight-lines are actually associated with the CGM of massive star-forming galaxies. This result is also consistent with the fact that on average, MgII absorbers have approximately solar metallicity at $z \sim 1$ (Lan & Fukugita 2017).

4.3. Outflow rate

As shown in Figure 8, the amount of neutral hydrogen mass within 100 kpc around ELGs exceeds from that around LRGs by about $2 \times 10^9 M_\odot$. Assuming that this mass difference is due to mass ejected from star-forming galaxies, we can estimate an outflow rate. We assume that the outflow material has a typical velocity of 200 km/s and typically travels a distance of ~ 100 kpc. The corresponding time scale is then about 500 Myr. If the excess mass around ELGs is assumed to be ejected about 500 Myr ago, we can estimate the outflow rate to be

$$\dot{M}_{\text{out}} = dM/dt \sim 2 \times 10^9 M_\odot / 500 \text{ Myr} \sim 4 M_\odot \text{ yr}^{-1}. \quad (8)$$

This estimated value should be considered as a lower limit, as about 80% of the excess mass is within 60 kpc, where the outflow velocity is lower than the typical outflow velocity. In addition, only cool gas clouds traced by MgII absorption are included, and a fraction of outflow materials may have already fallen back to the galaxies or been destroyed. Assuming that the SFR of the galaxies does not evolve significantly over 500 Myr, we can obtain a constraint on the minimum outflow loading factor:

$$\frac{\dot{M}_{\text{out}}}{\text{SFR}} > 4/8 \sim 0.5, \quad (9)$$

a value similar to the one obtained from the blue-shifted absorption lines towards galaxies (e.g. Rubin et al. 2014).

4.4. Comparison with previous studies

The absorption profile for ELGs at redshift 0.8 can be compared with that around Lyman break galaxies (LBGs) at redshift 2.2. To do this, we use the $\text{CII}\lambda 1334$ absorption strength obtained from Steidel et al. (2010) and convert it to the corresponding MgII absorption using $W_{\text{MgII,all}} \sim 3 \times W_{\text{CII}\lambda 1334}$ as given in Lan & Fukugita (2017). We find that at $r_p \sim 50$ kpc, the absorption around LBGs ($\sim 2 \text{ \AA}$) appears to be stronger than that around ELGs ($\sim 1 \text{ \AA}$), indicating a possible evolution of gas around star-forming galaxies. Unfortunately, the LBG data is still too uncertain to provide quantitative constraints on the evolution. We also compare our measurements with similar measurements from Rubin et al. (2018) and Bordoloi et al. (2011), both using spectra of galaxies as background sources. These measurements appear to be lower than ours but have large uncertainties. The difference could be due to that (1) their foreground star-forming galaxies have, on average, lower stellar masses and (2) they use extended objects as background sources, which may probe a larger region per line of sight as compared with quasars (see, Bordoloi et al. 2011, for a discussion).

4.5. Origins of the MgII/FeII absorption gas

Our results show that the properties of the cool gas around ELGs and LRGs are different. The gas profile between 10 kpc to 1 Mpc around LRGs is consistent with the NFW profile for dark matter distribution, as shown in Zhu et al. (2014), which can be described roughly by a power law. In contrast, the gas profile around ELGs is much steeper at impact parameters below 100 kpc, although it is comparable to that of LRGs at larger impact parameters. The properties of the absorbing gas is also found to be correlated with the star-formation activity and the azimuthal angle, with the absorption strength being stronger around ELGs with higher SFR and for sight-lines closer to the minor axes of the galaxies. In addition, the gas around star-forming galaxies appear to be stirred up in their halos than that around passive galaxies after normalizing the effect of halo mass. These results clearly have important implications for the origins of the absorption gas. In what follows, we discuss two possible mechanisms.

Gas associated with outflows - We argue that most of the cool gas around star-forming galaxies traced by MgII/FeII absorption lines within the halos is associated with outflows. Star-forming galaxies are known to eject gas via outflows. Evidence for such flows can be seen directly from the blue-shifted absorption lines in the galaxy spectra, i.e. through the so-called down-the-barrel observations (e.g., Weiner et al. 2009; Steidel et al. 2010; Martin et al. 2012; Bordoloi et al. 2014; Rubin et al. 2014; Zhu et al. 2015; Chisholm et al. 2016). However, the lack of spatial information in such observations makes it difficult to infer how far the gas associated with outflows can propagate into the halos. The azimuthal angle dependence of gas absorption found here is consistent with the scenario that the CGM is enriched by outflows. The azimuthal angle dependence is difficult to be explained by gas inflows and/or gas associated with satellite galaxies, because the gas distribution produced by such mechanisms is not expected to be aligned with

the minor axes of galaxies. Indeed, although the accretion of material from the cosmic web into dark matter halos is anisotropic (e.g., Shi et al. 2015), the alignment between the principal axes of late type galaxies and the cosmic web is found to be weak (e.g., Zhang et al. 2013), so is the alignment of late type galaxies with the distribution of satellite galaxies (e.g., Yang et al. 2006). We conclude, therefore, that the CGM around star-forming galaxies are produced and enriched by outflows driven by star formation in the galaxies.

The outflow gas traced by MgII around massive star-forming galaxies seems to have a characteristic scale of about 50-100 kpc (see also Bordoloi et al. 2011). This indicates that the bulk of the outflow materials in the cool phase cannot travel much farther than ~ 100 kpc from the central galaxies. This characteristic scale is an important observational constraint on any models of galactic outflows.

Gas associated with halos - We argue that, in addition to galactic outflows, a fraction of the MgII/FeII absorbing gas originates from mechanisms associated with halos of galaxies. This is motivated by the fact that a non-negligible amount of cool gas is found around LRGs, a population with no significant star formation activity over the past 1-2 Gyr or even longer (e.g., Barber et al. 2007; Gauthier & Chen 2011). Furthermore, the cool gas around LRGs has a relatively low velocity dispersion, and a distribution consistent with the NFW matter distribution without significant azimuthal dependence, all consistent with a halo origin. In the following, we discuss two possible mechanisms that may produce absorbing clouds in halos of galaxies. These mechanisms may also operate around star-forming galaxies, given that all galaxies are surrounded by extended halos.

One possibility is that the absorbing clouds originate from satellite galaxies. These galaxies are known to roughly trace the dark matter distribution (e.g., Lin et al. 2004), which may explain the observed gas density profile around LRGs. Before being accreted into their host halos, star-forming satellite galaxies have cool gas halos enriched by outflows, as discussed above. After merging into its host halo, a satellite may lose a fraction of the cool CGM due to ram pressure and/or tidal stripping, but it may still retain part of the CGM. Before being destroyed by hydro-dynamical instabilities and/or heat evaporation, both the remaining and stripped circumgalactic gas can contribute to the cool gas seen around LRGs. In addition, gas clouds may also be produced by the mass loss from evolved stars in the satellites. Under the assumption that satellite galaxies can retain *all of their cool CGM* without being destroyed or removed by any mechanisms, it seems possible to explain the observed MgII gas profiles observed around galaxy groups and LRGs by the gas associated with satellites (e.g., Bordoloi et al. 2011; Huang et al. 2016). However, if most of the absorbing gas were still bound to satellite galaxies, the gas kinematics would follow that of the satellites, and therefore that of dark matter (e.g., More et al. 2011), inconsistent with the observed gas kinematics. On the other hand, lower cloud velocity dispersion is expected for the clouds unbound to satellites, as ram pressure can decelerate them and hydrodynamic instabilities tend to destroy faster moving clouds in shorter time scales (see §3.4).

The cooling gas condensed from hot diffuse halos through thermal instability is another possible source for the MgII gas around LRGs. This scenario was first proposed by Mo & Miralda-Escude (1996), with an extension developed by Maller & Bullock (2004), and it assumes that a significant amount of hot gas within the cooling radius will condense into cool gas clouds. Given that the cooling time strongly depends on gas metallicity, it is expected that the high metallicity regions in the hot halos will cool first and produce gas clouds with high metal content. In addition, the condensed cool gas clouds are expected to have velocities modulated by the gravity of the systems and by the ram pressure of the hot halos, probably leading to low velocity dispersion. These two properties, high metallicity and low velocity dispersion, are consistent with the observed properties of the MgII gas, as shown in this paper and in Lan & Fukugita (2017). However, it is still unclear if this mechanism can produce the observed gas distribution.

It is possible that all the mechanisms discussed above can contribute to the cool gas around LRGs. The question that remains unsolved is their relative importance. By studying the contribution of each mechanism in detail through analytic and numerical models, it is possible to disentangle the origins of the cool gas around LRGs without the complications introduced by outflows. Thus, the gas properties around passive galaxies may provide a cleaner test bed for CGM models based on the halo origin than that around star-forming galaxies.

5. SUMMARY

The circumgalactic medium is expected to contain important information about gas accretion into galaxies, as well as gas flow processes that drive the evolution of galaxies. To reveal the imprints of these processes, we measure the distribution and kinematics of cool gas around star-forming and passive galaxies, using MgII/FeII absorption properties extracted from the flux decrements in the spectra of background quasars around $\sim 200,000$ ELGs and $\sim 800,000$ LRGs. Our findings can be summarized as follows:

1. ELGs appear to be surrounded by more cool gas than LRGs within 100 kpc despite being much less massive. The MgII and FeII absorption around ELGs is about 5-10 times stronger than around LRGs, and is stronger around ELGs with higher SFR. At larger scales, in contrast, the absorption around ELGs and LRGs has a similar strength and decreases with impact parameters following a power law, r_p^{-1} .
2. The metal absorption distribution around ELGs is anisotropic; for impact parameters below ~ 100 kpc, the metal absorption along the minor axes of ELGs is, on average, about two times stronger than that along the major axis. This indicates that a significant fraction of the absorbing gas, $\sim 2/3$, is probably generated by outflows from the galaxies.
3. The line-of-sight gas velocity dispersion σ_{gas} around ELGs and LRGs within 200 kpc is measured to be about 100 km/s and 160 km/s from the absorption line widths, respectively. Comparing these with the expected velocity dispersion of

dark matter particles, σ_m , in the host halos, we find that the gas moves differently around ELGs and LRGs, with the gas velocity bias

$$\frac{\sigma_{\text{gas}}}{\sigma_m} \sim \begin{cases} 1 & \text{for ELGs;} \\ 0.5 & \text{for LRGs.} \end{cases} \quad (10)$$

4. We infer the covering fraction of individual MgII absorbers and estimate the amount of neutral hydrogen around ELGs and LRGs based on an empirical relation between MgII strength and neutral hydrogen column density N_{HI} . Within 100 kpc, the neutral hydrogen mass around ELGs is about $2 \times 10^9 M_\odot$, about a factor of 3 more than that around LRGs. Assuming this difference is contributed by outflow materials, we constrain the minimum outflow loading factor to be about 0.5.

Our results demonstrate that the properties of cool gas around ELGs and LRGs within 100 kpc are significantly different in terms of their metal absorption profiles, gas abundance, and kinematics. This correlation between the gas properties and the SFR of galaxies is consistent with the picture that the CGM is enriched by metal-rich gas ejected via galactic outflows associated with recent star formation activities. Thus, the observed properties of the cool gas around star-forming galaxies can provide essential constraints on the feedback processes in galaxy formation. In a forthcoming paper (Lan et al. in preparation), we will use these results, together with a semi-analytic model for gaseous galactic halos, to constrain how the gas flow from galaxies can affect the circumgalactic media.

Our results also demonstrate the potential to measure the gas properties around galaxies with unprecedented precision by combining large samples and powerful statistical technique. Indeed, the large sample provided by SDSS already makes it possible to measure both the gas absorption towards ELGs ('down-the-barrel' observation, Zhu et al. 2015) and the gas absorption around ELGs robustly. With the advents of even larger and deeper spectroscopic samples of galaxies, such as DESI (Schlegel et al. 2011; Levi et al. 2013), PFS (Takada et al. 2014), Euclid (Amiaux et al. 2012), SDSS-V (Kollmeier et al. 2017), 4MOST (de Jong et al. 2016) and MOONS (Cirasuolo & MOONS Consortium 2016), we will be able to use more absorption species (MgII, FeII, CIV, etc) to probe the cosmic evolution of the circumgalactic gas-galaxy interaction, eventually obtaining a complete picture of baryon cycle in galaxy formation and evolution. In addition, it is also possible to use the galaxy-metal line cross-correlation to study the large-scale structure and even to detect the BAO signal (e.g., Blomqvist et al. 2018).

We thank Brice Ménard for his substantial suggestions on the manuscript, J.Xavier Prochaska for useful discussions, Nikole Nielsen for providing the kinematics data of her MgII absorber catalog, Dustin Lang for his helps on calculating the azimuthal angle, and Guangtun Zhu for sharing the NMF eigen-spectra of SDSS quasars. We also want to thank the anonymous referee for the constructive report. HJM acknowledges support from NSF AST-1517528, and from National Science Foundation of

China (grant Nos. 11673015, 11733004). Kavli IPMU is supported by World Premier International Research Center Initiative of the Ministry of Education, Japan.

Funding for the Sloan Digital Sky Survey IV has been provided by the Alfred P. Sloan Foundation, the U.S. Department of Energy Office of Science, and the Participating Institutions. SDSS acknowledges support and resources from the Center for High-Performance Computing at the University of Utah. The SDSS web site is www.sdss.org.

SDSS is managed by the Astrophysical Research Consortium for the Participating Institutions of the SDSS Collaboration including the Brazilian Participation Group, the Carnegie Institution for Science, Carnegie Mellon University, the Chilean Participation Group, the French Participation Group, Harvard-Smithsonian Center for Astrophysics, Instituto de Astrofísica de Canarias, The Johns Hopkins University, Kavli Institute for the Physics and Mathematics of the Universe (IPMU) / University of Tokyo, Lawrence Berkeley National Laboratory, Leibniz Institut für Astrophysik Potsdam (AIP), Max-Planck-Institut für Astronomie (MPIA Heidelberg), Max-Planck-Institut für Astrophysik (MPA Garching), Max-Planck-Institut für Extraterrestrische Physik (MPE), National Astronomical Observatories of China, New Mexico State University, New York University, University of Notre Dame, Observatorio Nacional / MCTI, The Ohio State University, Pennsylvania State University, Shanghai Astronomical Observatory, United Kingdom Participation Group, Universidad Nacional Autónoma de México, University of Arizona, University of Colorado Boulder, University of Oxford, University of Portsmouth, University of Utah, University of Virginia, University of Washington, University of Wisconsin, Vanderbilt University, and Yale University.

The Legacy Surveys consist of three individual and complementary projects: the Dark Energy Camera Legacy Survey (DECaLS; NOAO Proposal ID # 2014B-0404; PIs: David Schlegel and Arjun Dey), the Beijing-Arizona Sky Survey (BASS; NOAO Proposal ID # 2015A-0801; PIs: Zhou Xu and Xiaohui Fan), and the Mayall z-band Legacy Survey (MzLS; NOAO Proposal ID # 2016A-0453; PI: Arjun Dey). DECaLS, BASS and MzLS together include data obtained, respectively, at the Blanco telescope, Cerro Tololo Inter-American Observatory, National Optical Astronomy Observatory (NOAO); the Bok telescope, Steward Observatory, University of Arizona; and the Mayall telescope, Kitt Peak National Observatory, NOAO. The Legacy Surveys project is honored to be permitted to conduct astronomical research on Iolkam Du'ag (Kitt Peak), a mountain with particular significance to the Tohono O'odham Nation.

NOAO is operated by the Association of Universities for Research in Astronomy (AURA) under a cooperative agreement with the National Science Foundation.

This project used data obtained with the Dark Energy Camera (DECam), which was constructed by the Dark Energy Survey (DES) collaboration. Funding for the DES Projects has been provided by the U.S. Department of Energy, the U.S. National Science Foundation, the Ministry of Science and Education of Spain, the Science and Technology Facilities Council of the United Kingdom, the Higher Education Funding Council for England, the National Center for Supercomputing Applications

at the University of Illinois at Urbana-Champaign, the Kavli Institute of Cosmological Physics at the University of Chicago, Center for Cosmology and Astro-Particle Physics at the Ohio State University, the Mitchell Institute for Fundamental Physics and Astronomy at Texas A&M University, Financiadora de Estudos e Projetos, Fundação Carlos Chagas Filho de Amparo, Financiadora de Estudos e Projetos, Fundação Carlos Chagas Filho de Amparo a Pesquisa do Estado do Rio de Janeiro, Conselho Nacional de Desenvolvimento Científico e Tecnológico and the Ministerio da Ciencia, Tecnologia e Inovação, the Deutsche Forschungsgemeinschaft and the Collaborating Institutions in the Dark Energy Survey. The Collaborating Institutions are Argonne National Laboratory, the University of California at Santa Cruz, the University of Cambridge, Centro de Investigaciones Energéticas, Medioambientales y Tecnológicas-Madrid, the University of Chicago, University College London, the DES-Brazil Consortium, the University of Edinburgh, the Eidgenössische Technische Hochschule (ETH) Zurich, Fermi National Accelerator Laboratory, the University of Illinois at Urbana-Champaign, the Institut de Ciències de l'Espai (IEEC/CSIC), the Institut de Física d'Altes Energies, Lawrence Berkeley National Laboratory, the Ludwig-Maximilians Universität München and the associated Excellence Cluster Universe, the University of Michigan, the National Optical Astronomy Observatory, the University of Nottingham, the Ohio State University, the University of Pennsylvania, the University of Portsmouth, SLAC National Accelerator Laboratory, Stanford University, the University of Sussex, and Texas A&M University.

BASS is a key project of the Telescope Access Program (TAP), which has been funded by the National Astronomical Observatories of China, the Chinese Academy of Sciences (the Strategic Priority Research Program "The Emergence of Cosmological Structures" Grant # XDB09000000), and the Special Fund for Astronomy from the Ministry of Finance. The BASS is also supported by the External Cooperation Program of Chinese Academy of Sciences (Grant # 114A11KYSB20160057), and Chinese National Natural Science Foundation (Grant # 11433005).

The Legacy Survey team makes use of data products from the Near-Earth Object Wide-field Infrared Survey Explorer (NEOWISE), which is a project of the Jet Propulsion Laboratory/California Institute of Technology. NEOWISE is funded by the National Aeronautics and Space Administration.

The Legacy Surveys imaging of the DESI footprint is supported by the Director, Office of Science, Office of High Energy Physics of the U.S. Department of Energy under Contract No. DE-AC02-05CH1123, by the National Energy Research Scientific Computing Center, a DOE Office of Science User Facility under the same contract; and by the U.S. National Science Foundation, Division of Astronomical Sciences under Contract No. AST-0950945 to NOAO.

REFERENCES

- Abolfathi, B., Aguado, D. S., Aguilar, G., et al. 2018, *ApJS*, 235, 42
- Amiaux, J., Scaramella, R., Mellier, Y., et al. 2012, *Proc. SPIE*, 8442, 84420Z

- Barber, T., Meiksin, A., & Murphy, T. 2007, *MNRAS*, 377, 787
- Bergeron, J. 1986, *A&A*, 155, L8
- Blanton, M. R., Bershad, M. A., Abolfathi, B., et al. 2017, *AJ*, 154, 28
- Blomqvist, M., Pieri, M. M., du Mas des Bourboux, H., et al. 2018, *arXiv:1801.01852*
- Bolton, A. S., Schlegel, D. J., Aubourg, É., et al. 2012, *AJ*, 144, 144
- Bordoloi, R., Lilly, S. J., Knobel, C., et al. 2011, *ApJ*, 743, 10
- Bordoloi, R., Lilly, S. J., Hardmeier, E., et al. 2014, *ApJ*, 794, 130
- Bordoloi, R., Tumlinson, J., Werk, J. K., et al. 2014, *ApJ*, 796, 136
- Bordoloi, R., Prochaska, J. X., Tumlinson, J., et al. 2017, *arXiv:1712.02348*
- Borthakur, S., Heckman, T., Tumlinson, J., et al. 2016, *ApJ*, 833, 259
- Bouché, N., Hohensee, W., Vargas, R., et al. 2012, *MNRAS*, 426, 801
- Burchett, J. N., Tripp, T. M., Bordoloi, R., et al. 2016, *ApJ*, 832, 124
- Chen, H.-W., Helsby, J. E., Gauthier, J.-R., et al. 2010, *ApJ*, 714, 1521
- Chisholm, J., Tremonti, C. A., Leitherer, C., Chen, Y., & Wofford, A. 2016, *MNRAS*, 457, 3133
- Churchill, C. W., & Vogt, S. S. 2001, *AJ*, 122, 679
- Churchill, C. W., Vogt, S. S., & Charlton, J. C. 2003, *AJ*, 125, 98
- Churchill, C. W., Kacprzak, G. G., & Steidel, C. C. 2005, *IAU Colloq. 199: Probing Galaxies through Quasar Absorption Lines*, 24
- Churchill, C. W., Nielsen, N. M., Kacprzak, G. G., & Trujillo-Gomez, S. 2013, *ApJL*, 763, L42
- Comparat, J., Delubac, T., Jouvel, S., et al. 2016, *A&A*, 592, A121
- Conroy, C., Wechsler, R. H., & Kravtsov, A. V. 2006, *ApJ*, 647, 201
- Cirasuolo, M., & MOONS Consortium 2016, *Multi-Object Spectroscopy in the Next Decade: Big Questions, Large Surveys, and Wide Fields*, 507, 109
- de Jong, R. S., Barden, S. C., Bellido-Tirado, O., et al. 2016, *Proc. SPIE*, 9908, 99081O
- Dawson, K. S., Schlegel, D. J., Ahn, C. P., et al. 2013, *AJ*, 145, 10
- Dawson, K. S., Kneib, J.-P., Percival, W. J., et al. 2016, *AJ*, 151, 44
- Dey, A., Schlegel, D. J., Lang, D., et al. 2018, *arXiv:1804.08657*
- Elahi, P. J., Power, C., Lagos, C. d. P., Poulton, R., & Robotham, A. S. G. 2018, *MNRAS*
- Favole, G., Comparat, J., Prada, F., et al. 2016, *MNRAS*, 461, 3421
- Gauthier, J.-R., & Chen, H.-W. 2011, *MNRAS*, 418, 2730
- Gunn, J. E., Siegmund, W. A., Mannery, E. J., et al. 2006, *AJ*, 131, 2332
- Heckman, T. M., Lehnert, M. D., Strickland, D. K., & Armus, L. 2000, *ApJS*, 129, 493
- Heckman, T. M., Alexandroff, R. M., Borthakur, S., Overzier, R., & Leitherer, C. 2015, *ApJ*, 809, 147
- Heckman, T., Borthakur, S., Wild, V., Schiminovich, D., & Bordoloi, R. 2017, *ApJ*, 846, 151
- Ho, S. H., Martin, C. L., Kacprzak, G. G., & Churchill, C. W. 2017, *ApJ*, 835, 267
- Huang, Y.-H., Chen, H.-W., Johnson, S. D., & Weiner, B. J. 2016, *MNRAS*, 455, 1713
- Hutchinson, T. A., Bolton, A. S., Dawson, K. S., et al. 2016, *AJ*, 152, 205
- Johnson, S. D., Chen, H.-W., Mulchaey, J. S., Schaye, J., & Straka, L. A. 2017, *ApJL*, 850, L10
- Kacprzak, G. G., & Churchill, C. W. 2011, *ApJL*, 743, L34
- Kacprzak, G. G., Churchill, C. W., & Nielsen, N. M. 2012, *ApJL*, 760, L7
- Kennicutt, R. C., Jr. 1998, *ARA&A*, 36, 189
- Kollmeier, J. A., Zasowski, G., Rix, H.-W., et al. 2017, *arXiv:1711.03234*
- Lan, T.-W., Ménard, B., & Zhu, G. 2014, *ApJ*, 795, 31
- Lan, T.-W., & Fukugita, M. 2017, *ApJ*, 850, 156
- Lan, T.-W., Ménard, B., Baron, D., et al. 2018, *MNRAS*, 477, 3520
- Lang, D., Hogg, D. W., & Mykytyn, D. 2016, *Astrophysics Source Code Library*, ascl:1604.008
- Lee, D. D., & Seung, H. S. 2001, in *Advances in neural information processing systems*, 556562
- Levi, M., Bebek, C., Beers, T., et al. 2013, *arXiv:1308.0847*
- Liang, C. J., & Chen, H.-W. 2014, *MNRAS*, 445, 2061
- Lin, Y.-T., Mohr, J. J., & Stanford, S. A. 2004, *ApJ*, 610, 745
- Lopez, S., Tejos, N., Ledoux, C., et al. 2018, *Nature*, 554, 493
- Maller, A. H., & Bullock, J. S. 2004, *MNRAS*, 355, 694
- Martin, C. L., Shapley, A. E., Coil, A. L., et al. 2012, *ApJ*, 760, 127
- Ménard, B., Wild, V., Nestor, D., et al. 2011, *MNRAS*, 417, 801
- Ménard, B., & Fukugita, M. 2012, *ApJ*, 754, 116
- Mo, H. J., & Miralda-Escude, J. 1996, *ApJ*, 469, 589
- Mo, H., van den Bosch, F. C., & White, S. 2010, *Galaxy Formation and Evolution*, by Houjun Mo, Frank van den Bosch, Simon White, Cambridge, UK: Cambridge University Press, 2010,
- More, S., van den Bosch, F. C., Cacciato, M., et al. 2011, *MNRAS*, 410, 210
- Moustakas, J., Coil, A. L., Aird, J., et al. 2013, *ApJ*, 767, 50
- Navarro, J. F., Frenk, C. S., & White, S. D. M. 1996, *ApJ*, 462, 563
- Nestor, D. B., Turnshek, D. A., & Rao, S. M. 2005, *ApJ*, 628, 637
- Nielsen, N. M., Churchill, C. W., Kacprzak, G. G., & Murphy, M. T. 2013, *ApJ*, 776, 114
- Nielsen, N. M., Churchill, C. W., Kacprzak, G. G., Murphy, M. T., & Evans, J. L. 2015, *ApJ*, 812, 83
- Nielsen, N. M., Churchill, C. W., Kacprzak, G. G., Murphy, M. T., & Evans, J. L. 2016, *ApJ*, 818, 171
- Pâris, I., Petitjean, P., Aubourg, E., et al. 2017, *arXiv:1712.05029*
- Peek, J. E. G., Ménard, B., & Corrales, L. 2015, *ApJ*, 813, 7
- Prakash, A., Licquia, T. C., Newman, J. A., et al. 2016, *ApJS*, 224, 34
- Prochaska, J. X., Lau, M. W., & Hennawi, J. F. 2014, *ApJ*, 796, 140
- Prochaska, J. X., Werk, J. K., Worseck, G., et al. 2017, *ApJ*, 837, 169
- Raichoor, A., Comparat, J., Delubac, T., et al. 2016, *A&A*, 585, A50
- Raichoor, A., Comparat, J., Delubac, T., et al. 2017, *MNRAS*, 471, 3955
- Rubin, K. H. R., Prochaska, J. X., Koo, D. C., et al. 2014, *ApJ*, 794, 156
- Rubin, K. H. R., Diamond-Stanic, A. M., Coil, A. L., Crighton, N. H. M., & Moustakas, J. 2018, *ApJ*, 853, 95
- Schlegel, D., Abdalla, F., Abraham, T., et al. 2011, *arXiv:1106.1706*
- Schroetter, I., Bouché, N., Wendt, M., et al. 2016, *ApJ*, 833, 39
- Shi, J., Wang, H., & Mo, H. J. 2015, *ApJ*, 807, 37
- Smee, S. A., Gunn, J. E., Uomoto, A., et al. 2013, *AJ*, 146, 32
- Steidel, C. C., Dickinson, M., & Persson, S. E. 1994, *ApJL*, 437, L75
- Steidel, C. C., Erb, D. K., Shapley, A. E., et al. 2010, *ApJ*, 717, 289
- Stocke, J. T., Keeney, B. A., Danforth, C. W., et al. 2013, *ApJ*, 763, 148
- Takada, M., Ellis, R. S., Chiba, M., et al. 2014, *PASJ*, 66, R1
- Tumlinson, J., Thom, C., Werk, J. K., et al. 2011, *Science*, 334, 948
- Tumlinson, J., Thom, C., Werk, J. K., et al. 2013, *ApJ*, 777, 59
- Tumlinson, J., Peebles, M. S., & Werk, J. K. 2017, *ARA&A*, 55, 389
- Veilleux, S., Cecil, G., & Bland-Hawthorn, J. 2005, *ARA&A*, 43, 769
- Weiner, B. J., Coil, A. L., Prochaska, J. X., et al. 2009, *ApJ*, 692, 187
- Werk, J. K., Prochaska, J. X., Tumlinson, J., et al. 2014, *ApJ*, 792, 8
- White, M., Blanton, M., Bolton, A., et al. 2011, *ApJ*, 728, 126
- Yang, X., van den Bosch, F. C., Mo, H. J., et al. 2006, *MNRAS*, 369, 1293
- Zhai, Z., Tinker, J. L., Hahn, C., et al. 2017, *ApJ*, 848, 76
- Zhang, Y., Yang, X., Wang, H., et al. 2013, *ApJ*, 779, 160
- Zhu, G., & Ménard, B. 2013a, *ApJ*, 773, 16
- Zhu, G., & Ménard, B. 2013b, *ApJ*, 770, 130
- Zhu, G., Ménard, B., Bizyaev, D., et al. 2014, *MNRAS*, 439, 3139

Zhu, G. B., Comparat, J., Kneib, J.-P., et al. 2015, ApJ, 815, 48
Zhu, G. 2016, arXiv:1612.06037

Zibetti, S., Ménard, B., Nestor, D. B., et al. 2007, ApJ, 658, 161